Available online at www.sciencedirect.com

SciVerse ScienceDirect

Ceramics International 39 (2013) 6637–6646

CERAMICS INTERNATIONAL

www.elsevier.com/locate/ceramint

Spark plasma sintering of graphene reinforced zirconium diboride ultra-high temperature ceramic composites

Govindaraajan B. Yadhukulakrishnan, Sriharsha Karumuri, Arif Rahman, Raman P. Singh, A. Kaan Kalkan, Sandip P. Harimkar*

School of Mechanical and Aerospace Engineering Oklahoma State University, Stillwater, OK 74078, USA

Received 8 January 2013; received in revised form 14 January 2013; accepted 15 January 2013
Available online 6 February 2013

Abstract

Spark plasma sintering (SPS) of monolithic ZrB_2 ultra-high temperature ceramic and 2–6 vol% graphene nanoplates (GNPs) reinforced ZrB_2 matrix composites is reported. The SPS at 1900 °C with a uni-axial pressure of 70 MPa and soaking time of 15 min resulted in near-full densification in ZrB_2–GNP composites. Systematic investigations on the effect of GNP reinforcement on densification behavior, microstructure, and mechanical properties (microhardness, biaxial flexural strength, and indentation fracture toughness) of the composites are presented. Densification mechanisms, initiated by interfacial reactions, are also proposed based on detailed thermodynamic analysis of possible reactions at the sintering temperature and the analysis of in-process punch displacement profiles. The results show that GNPs can be retained in the ZrB_2 matrix composites even with high SPS temperature of 1900 °C and cause toughening of the composites through a range of toughening mechanisms, including GNP pull-out, crack deflection, and crack bridging.

Keywords: A. Sintering; B. Composites; B. Microstructure-final; C. Toughness and toughening; D. Borides

1. Introduction

Ceramics with melting point greater than 3200 °C are generally classified as ultra-high temperature ceramics (UHTC). The most important application of UHTC is in the leading edges and nose caps of space vehicles re-entering the earth's atmosphere. These materials also find applications in high temperature crucibles and parts of electrical heaters and igniters [1–4]. Among the several UHTC systems (TaC, HfC, NbC, ZrC, HfB_2, ZrB_2, and TiB_2), ZrB_2 based ceramics are the most promising for thermal protection systems due to their good combination of elevated temperature mechanical properties and oxidation resistance. However, there is a critical need to further improve their oxidation resistance, thermal conductivity, and fracture toughness to realize the full potential of ZrB_2-based ceramics as next generation materials for sharp leading edge re-entry space vehicles [5–8]. In general, reinforcements are added to ZrB_2 ceramic matrix to improve sinterability and mechanical, thermal, and oxidation properties of the composites. Several investigations have reported improved oxidation resistance and/or fracture toughness of SiC reinforced ZrB_2 ceramic composites [9–14]. Recently, carbon nanotubes (CNTs) have also been used as nano-scale filler in the ZrB_2 ceramics [14–15]. The CNT reinforcement resulted in improved densification particularly in the early (particle rearrangement) and final stages (diffusion) of densification. The CNT reinforcement also resulted in improvement in room temperature fracture toughness [14]. While the effectiveness of CNT reinforcement in improving densification and fracture toughness was demonstrated, exact mechanisms of densification and toughening are still not fully understood. Furthermore, uniform dispersion of the CNTs in the UHTC composites is often difficult [16].

Recently, graphene nanoplates (GNPs) are attracting significant attention as potential nano-scale reinforcement

---

*Corresponding author. Tel.: +1 405 744 5830.
E-mail address: sandip.harimkar@okstate.edu (S.P. Harimkar).

0272-8842/$ - see front matter © 2013 Elsevier Ltd and Techna Group S.r.l. All rights reserved.
http://dx.doi.org/10.1016/j.ceramint.2013.01.101

in advanced composites. Graphene is a single atom thick sheet of sp^2 hybridized carbon atoms arranged in a honeycomb structure. It is the building block for other sp^2 hybridized carbon forms such as single and multi-walled CNTs. It also exhibits unique mechanical, electrical, and thermal properties [17–22]. These properties have also been extended in bi- and few-layer graphene [23–25]. Unlike CNTs, a fairly uniform distribution of GNPs is possible in the ceramic matrices using traditional processing approaches [26]. A number of studies have reported on reinforcement of GNPs to improve the mechanical properties of polymer, metals/alloys, and ceramic matrix composites [27–33]. Most recently, Walker et al. [31] used GNPs as nano-reinforcement in silicon nitride ceramic matrix composites. The GNP reinforcement significantly improved the fracture toughness of Si_3N_4 through a range of toughening mechanisms including wrapping of GNPs to resist sheet pull-out, crack bridging, and crack deflection. A three-dimensional crack deflection mechanism, induced by GNPs, for observed improved toughness of the ceramic matrix was also proposed [31]. As with CNT reinforcement, the mechanisms of densification in presence of GNPs are not well investigated. This is particularly important in case of high temperature sintering of high-melting point ceramics because of potential structural damage to the GNPs and consequent degradation of properties.

In this paper, spark plasma sintering (SPS) of GNP reinforced ZrB_2-based UHTCs is reported. Detailed investigations on the effect of GNP reinforcement on densification behavior, microstructure, and mechanical properties (micro-hardness, bi-axial flexural strength, and indentation fracture toughness) of the composites are presented. The SPS is a relatively novel process where powders are sintered under simultaneous influence of pulsed direct current and uni-axial pressure. While there is no general agreement on the nature of active sintering mechanisms during SPS, it is widely accepted that Joule heating at the particle contacts causes localized heating and solid state diffusion. Due to unique mechanisms of sintering, SPS often allows sintering at relatively lower temperature and in shorter sintering time compared to conventional hot pressing. In this investigation, in-process punch displacement profiles and thermodynamic analysis were used to seek better understanding of the densification mechanisms in presence of GNPs at sintering temperature of 1900 °C. Detailed results of Raman spectroscopy and SEM microscopy are also presented with critical analysis of structural changes in GNPs during SPS and potential toughening mechanisms in the ZrB_2–GNP composites.

2. Experimental procedure

Commercially available ZrB_2 powder (1–2 μm diameter; Alfa Aesar, USA) and graphene nanoplates (6–8 nm thick, 5 μm diameter; XG Sciences, USA) were used as starting materials for the processing of monolithic ZrB_2 and ZrB_2–GNP composites. ZrB_2–GNP composite powder mixtures, with 2, 4, and 6 vol% GNPs were prepared using colloidal processing [34]. Pre-measured quantity of GNPs was stirred in 100 ml acetone for 1.5 h using a high speed magnetic stirrer. ZrB_2 powder was then added into the mixture and stirred for additional 1.5 h. The slurry was then heated at 70 °C for 3 h using a hot plate followed by 24 h drying in a fume hood. Fully dried composite powder mixture was then milled in a high energy ball mill (Fritsch, USA) with a speed of 500 revolutions per minute and ball-to-powder weight ratio of 5:2 for 5 min. For preparing monolithic ZrB_2, as-received powder was ball milled with the milling parameters same as those for composite powder mixtures. Tungsten carbide (WC) balls and jar were used for ball milling. It has been reported that ball milling results in exfoliation of graphene into fewer or even single layer GNPs in the composite powder mixture [35]. The ball milled ZrB_2, ZrB_2–GNP composite powders were sintered at 1900 °C with a uniaxial pressure of 70 MPa and soaking time of 15 min under argon atmosphere using a commercial SPS system (Thermal Technology LLC, USA). Initial heating rate of 100 °C/min was used to attain sintering temperature of 1900 °C. Disc-shaped samples of 20 mm diameter and 2 mm thickness were sintered using graphite dies and punches. To investigate densification behavior of monolithic ZrB_2 and ZrB_2–GNP composites, punch displacement was continuously monitored during the SPS cycle. Archimedes′ principle was used to measure bulk densities of the sintered samples. The theoretical densities of the composites were calculated using the rule of mixtures. For phase analysis of the samples, a X-ray diffractometer (Philips Norelco, USA) operating with Cu K_α ($\lambda = 1.54178$ Å) radiation was used. Raman spectroscopy was carried out to characterize GNPs on the fracture surfaces of sintered composites using 532 nm laser excitation, 0.8 mW laser power, and 20 μm spot size (WITec Instruments Corp., Germany). A Vickers hardness tester (Clark Instrument, USA), operated with a normal force of 9.8 N and holding time of 15 s, was used to determine indentation hardness of the samples. The indentation fracture toughness of the samples was calculated by measuring lengths of diagonal cracks emanated at the indentation corners. The fracture toughness values are based on three samples with five indents per sample. The indentation fracture toughness, K_{IC}, is given by

$$K_{IC} = 0.016\left(\frac{E}{H}\right)^{1/2}\frac{P}{c^{3/2}}, \qquad (1)$$

where E is the Young's modulus of the composites (Young's moduli of ZrB_2 and GNP are 500 and 1000 GPa, respectively), H is the Vickers hardness (GPa), P is the applied load (N), and c is the diagonal crack length (m) [36]. The flexure strength for the samples, 20 mm in diameter and 2 mm in thickness, was determined using ASTM C1499-05 ring-on-ring test method (Instron, USA). The support and loading ring diameters were 15 mm and

Table 1
Relative density and mechanical properties.

Sample	Relative density (%)	Hardness (GPa)	Fracture toughness (MPa m$^{1/2}$)	Flexural strength (MPa)
ZrB_2	84.8	16.64 ± 0.90	1.51 ± 0.02	162 ± 31
ZrB_2+2% GNPs	84.5	13.53 ± 0.25	2.10 ± 0.43	204 ± 34
ZrB_2+4% GNPs	96.5	15.90 ± 0.84	2.15 ± 0.24	219 ± 23
ZrB_2+6% GNPs	96.9	14.00 ± 0.60	2.77 ± 0.06	316 ± 85

5 mm, respectively, with a displacement controlled loading rate of 0.5 mm/min. The flexure strength, σ_{RoR}, is given by

$$\sigma_{\mathrm{RoR}} = \frac{3P}{2\pi t^2}\left(\frac{(1-\upsilon)(a^2-r^2)}{2R^2}+(1+\upsilon)\ln\frac{a}{r}\right), \quad (2)$$

where P is the applied load (N), v is the Poisson's ratio of the composites (υ of ZrB_2 and GNP are 0.15 and 0.165, respectively), a is the radius of the support ring, r is the radius of the load ring (m), and R and t are the sample radius and thickness (m), respectively [37]. Three flexure tests were conducted for each sample condition and average values along with positive and negative error bars are reported. The fracture surfaces of the samples were analyzed using SEM to investigate microstructure development and fracture behavior. The relative density and mechanical properties of sintered monolithic ZrB_2 and ZrB_2–GNP composites are listed in Table 1.

3. Results and discussion

3.1. Densification behavior and microstructure development

Fig. 1 presents the variation of relative density of ZrB_2–GNP composite samples with GNP reinforcement content (0–6 vol%). The average relative density of monolithic ZrB_2 (0 vol% GNPs) and ZrB_2–GNP (2 vol% GNPs) composites was about 85%. For the similar SPS processing parameters (sintering temperature of 1900 °C, uniaxial pressure of 70 MPa, and soaking time of 15 min), the relative density of ZrB_2–GNP composites increased with GNP reinforcement content. The ZrB_2–GNP composites with 6 vol% GNPs exhibited highest relative density of about 97%. The SEM micrographs from the fracture surface of the ZrB_2 and ZrB_2–GNP composites are shown in Fig. 2. As seen in the figure, the monolithic ZrB_2 samples exhibited uniformly distributed porosity (relative density of about 85%) with average grain size of about 2.1 µm, which is slightly greater than starting ZrB_2 particle size (1–2 µm). The ZrB_2–GNP composite reinforced with 2 vol% GNPs had comparable density of about 85% and average grain size of about 2.3 µm. The ZrB_2–GNP composites reinforced with 4 and 6 vol% GNPs exhibited dense microstructure with relatively flatter features. Some distributed closed porosity and grain pull-out depressions can be seen on the fracture surfaces of these composite samples. The average grain size for these dense ZrB_2–GNP composites (4–6 vol% GNPs) was about 4.1–4.7 µm. Furthermore, the SEM micrographs clearly show distributed GNPs pulled out at the grain boundaries. Clearly, the reinforcement of GNPs above 2 vol% in ZrB_2 UHTC resulted in significant improvement in densification with minimal grain growth. Similar improvements in the densification of ZrB_2 UHTC were also observed with reinforcement of carbon nanotubes (CNTs) and carbon [14].

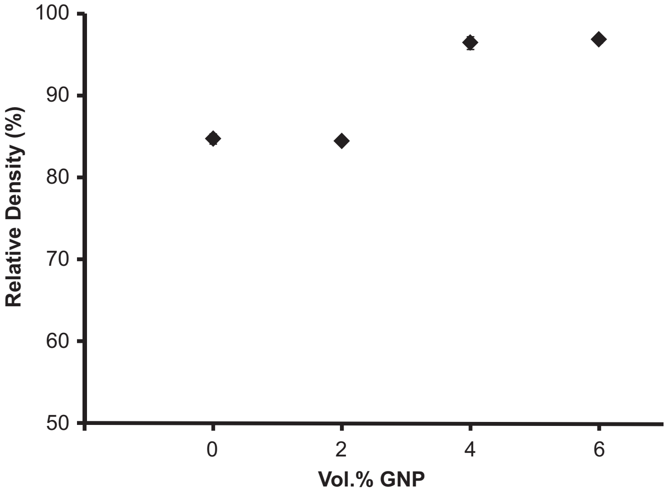

Fig. 1. Variation of relative density of ZrB_2–GNP composites with reinforcement content.

To get better insight into densification behavior of the monolithic ZrB_2 and ZrB_2–GNP composites, the data on punch displacement was recorded during SPS. The punch displacement profiles during initial heating and soaking stages of the SPS cycle for ZrB_2 and ZrB_2–GNP composites are shown in Fig. 3. The temperature and pressure profiles during sintering cycle are also plotted in the figure. Note that temperature and pressure were simultaneously increased during sintering. The desired pressure of 70 MPa was reached in first 8 min of the sintering cycle. The sintering temperature of 1900 °C was reached in first 17 min of the cycle. With the soaking time of 15 min, the total sintering time (heating and soaking stages) was about 32 min. The punch displacement profiles clearly indicate three distinct trends: initial increasing trend (compaction) corresponding to increasing pressure (stage I), intermediate decreasing trend corresponding to thermal expansion (stage II), and final increasing trend corresponding to final densification stages (stage III). It can be seen from the figure that initial compression in monolithic ZrB_2 was about 0.25 mm. This compression was significantly higher for ZrB_2–GNP composites reaching about 0.95 mm

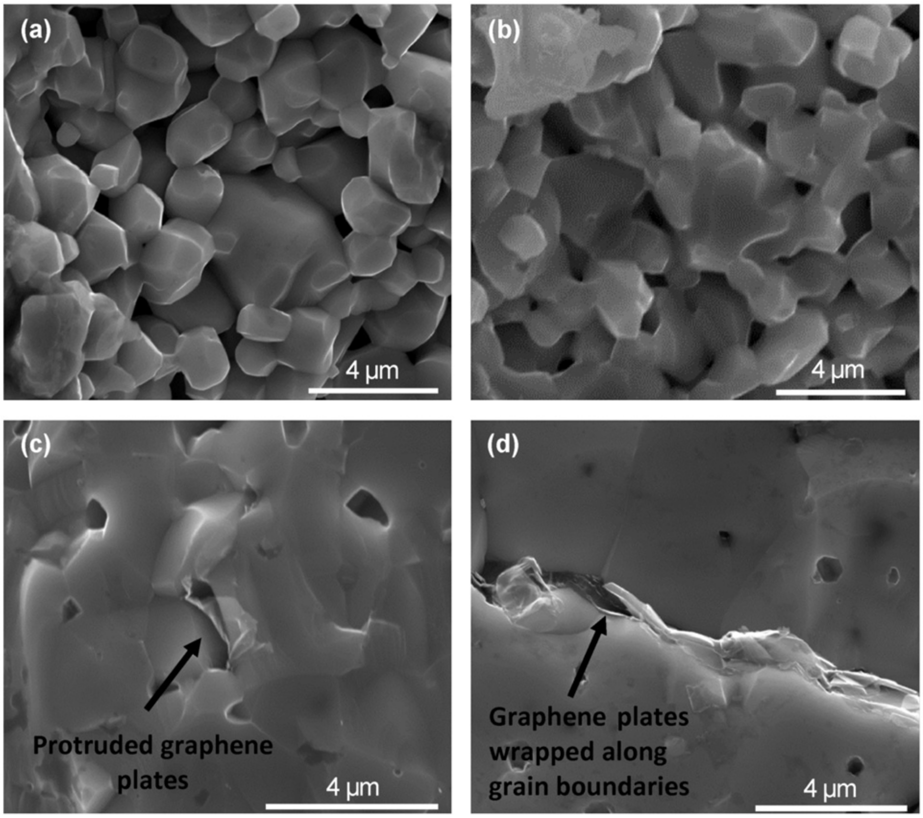

Fig. 2. SEM micrographs from the fracture surfaces of (a) monolithic ZrB_2, (b) ZrB_2+2 vol% GNPs, (c) ZrB_2+4 vol% GNPs, and (d) ZrB_2+6 vol% GNPs composites.

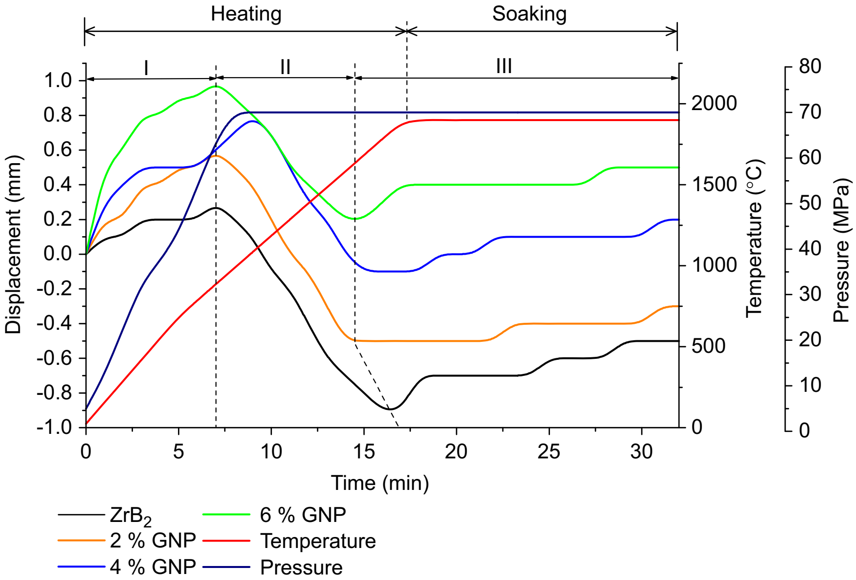

Fig. 3. Ram displacement, temperature, and pressure profiles during heating and soaking stages of SPS cycles for monolithic ZrB_2 and ZrB_2–GNP composites.

for composites reinforced with 6 vol% GNPs. While GNPs seem to promote early stages of densification dominated by particle re-arrangement, the GNPs also shift the stage II-III transition point to left (earlier times) indicating enhanced densification in later stages (indicated by dotted line). For the monolithic ZrB_2, the stage III densification begins at the start of soaking cycle at 1900 °C ($t=17$ min). This stage of densification begins in heating cycle at the temperature of about 1700 °C ($t\sim13$ min) for ZrB_2–GNP composites.

While the exact nature of mechanisms of densification in presence of GNPs is not fully understood, it seems that GNPs promote early stage ZrB_2 particle rearrangement due to its self lubricating effects. In the later stages of sintering of ZrB_2–GNP composites, GNPs act more as sintering aid. Carbon has long been used as a sintering aid for the densification of ceramics, and it is often proposed that carbon removes the native oxides on the surfaces of the non-oxide ceramics by some interfacial reactions and promote the densification. Zhu et al. reported nearfull densification of carbon-coated ZrB_2 ceramic using pressureless sintering and proposed possible interfacial reactions based on thermodynamic analysis. For ZrB_2 UHTC, the native oxides on the surfaces are ZrO_2 and B_2O_3. During high temperature sintering, GNPs can react with these native oxides according to carbothermal reduction reactions [38]:

$$ZrO_2+B_2O_3+5C \rightarrow ZrB_2+5CO \tag{3}$$

$$ZrO_2+3C \rightarrow ZrC+2CO \tag{4}$$

The free energies of these reactions are plotted over a range of temperatures from 0 to 3000 °C in the standard state (pressure ~1 atm) in Fig. 4. From these thermodynamic calculations, it can be seen that the reactions (3) and (4) are feasible at temperatures above 1500 and 1656 °C, respectively, in the standard state as long as the activation barrier is surmounted by the available thermal energy in the medium. With the reduced pressure during SPS, these reactions are expected to be feasible even at lower temperatures. According to these reactions, the surface oxides get converted back to ZrB_2 or form interfacial product (ZrC). The removal of oxide impurities in presence of graphene nanoplates possibly promotes densification in ZrB_2–GNP composites in later stages of sintering as indicated by punch displacement profiles. As the fracture surfaces showed intact GNPs at the grain boundaries, the surface reactions leading to enhanced densification seem to occur at ZrB_2/GNP interface.

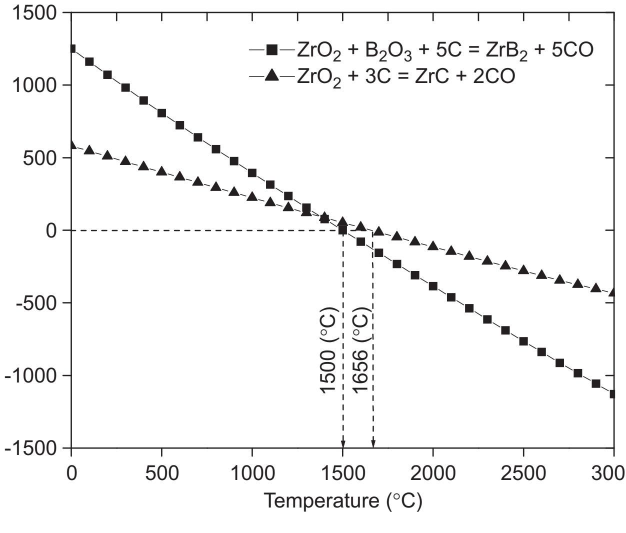

Fig. 4. Gibbs free energies of interfacial carbothermal reduction reactions as a function of temperature.

3.2. X-ray diffraction and Raman spectroscopy analysis

X-ray diffraction (XRD) patterns from sintered monolithic ZrB_2 and ZrB_2–GNP composites are presented in Fig. 5. While all the samples showed characteristic peaks of ZrB_2 in the XRD patterns, the characteristic (002) peak of graphene at $2\theta=26.6^\circ$ was not observed in the patterns from composites. Furthermore, no additional peaks corresponding to possible interfacial reaction product ZrC were observed. This is not surprising as the XRD analysis often does not show additional peaks when the reinforcement content is very low and the interfacial reactions are limited to near-interface regions. Furthermore, some of the interfacial products, possibly ZrC here, exhibit very high solubility in the matrix ZrB_2 phase and may not show up in XRD patterns.

Raman spectroscopy was also used to characterize ZrB_2–GNP composites. Raman acquisitions reveal the state of GNPs during the SPS of the composites. A typical graphitic carbon exhibit characteristic Raman peaks at D (1350 cm^{-1}) and G (1580 cm^{-1}) representing in-plane stretching and breathing modes, respectively, while the peaks at D' (1620 cm^{-1}) and G' (2700 cm^{-1}) are attributed to their respective higher order modes [39–41]. The modes corresponding to D and D' peaks are forbidden in the perfect sp^2 hybridized carbon due to symmetry. However, the presence of defects creates structural disorder that allows the breathing mode [39–41]. Hence, the D and D' peaks are observed only in graphitic carbon with disorder in its crystal structure. In the present study, we analyzed the characteristic Raman peaks of GNPs at the fractured surfaces of the composites. Fig. 6(a) shows the Raman spectra of ZrB_2–GNP composites (2, 4 and 6 vol% GNPs) along with sintered GNPs and ZrB_2. It is obvious from the Raman spectrum of ZrB_2 that it has no detectable Raman-active vibrational modes in the frequency range of 1000–3000 cm^{-1}. Hence, the Raman spectra acquired from the composites exhibit the characteristic peaks of GNPs. Further, it is apparent that the D and G peaks in ZrB_2–GNP

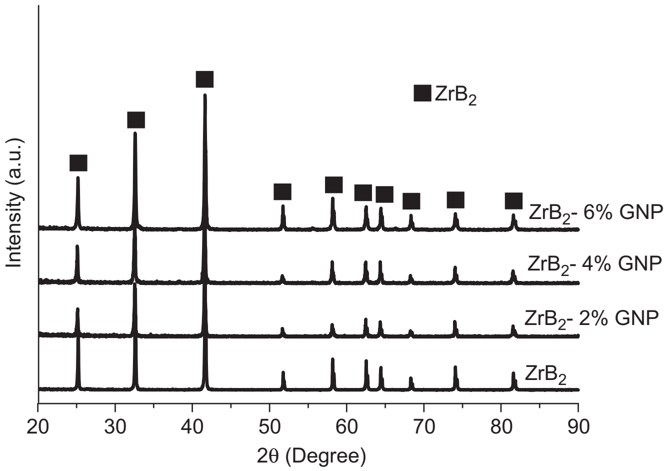

Fig. 5. XRD patterns from sintered ZrB_2 and ZrB_2–GNP composites.

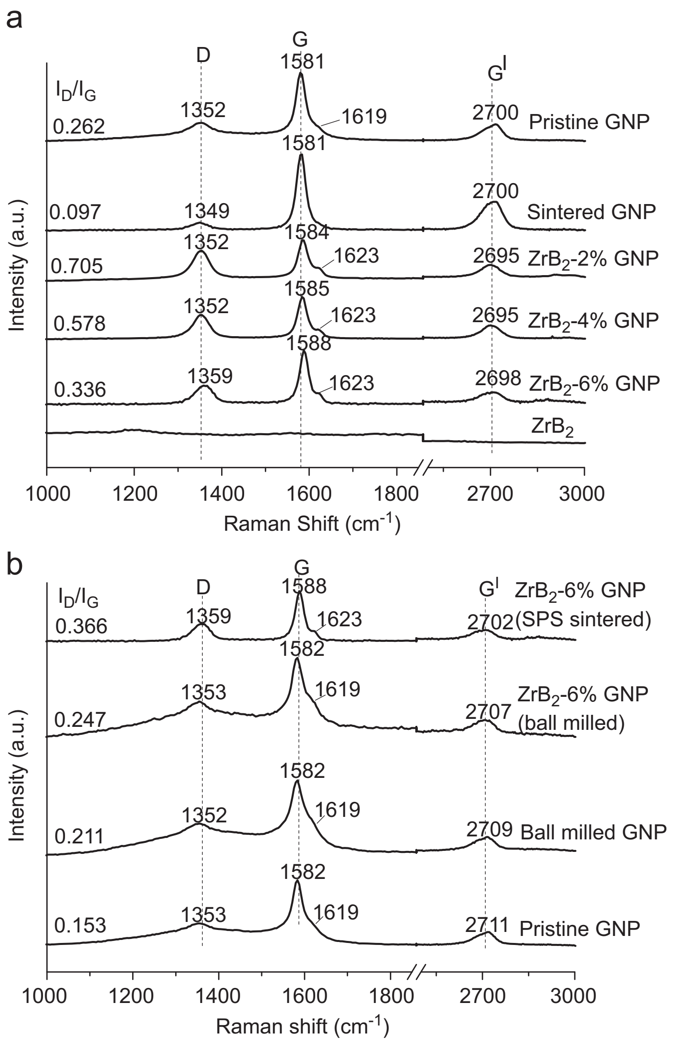

Fig. 6. Raman spectra of (a) ZrB$_2$, ZrB$_2$–GNP composites, pristine GNPs, and sintered GNPs; and (b) pristine GNPs, ball milled GNPs, ball milled ZrB$_2$–6% GNPs powder, and sintered ZrB$_2$–6% GNPs composite.

composites have shifted to higher energy, while the *G*′ band has shifted to lower energy. The position of *G* and *G*′ peaks are influenced by the following factors: (i) density of defects in the GNPs incurred during SPS processing [41], (ii) the thermal residual stress [42–44] that evolves during the cooling step (i.e., thermal contraction of ZrB$_2$ matrix surrounding GNPs), and (iii) reduction in number of graphene layers (nGLs) [45–46].

A routinely used measure of density of defects in graphitic carbon materials is the ratio of intensities of *D* to *G* peaks (I_D/I_G) [39,41]. I_D/I_G values for GNPs in ZrB$_2$–GNP composites (2, 4 and 6 vol% GNPs), sintered GNPs, and pristine GNPs are displayed in Fig. 6(a) (in fact, these values are close to average values of I_D/I_G). It is evident from the values of I_D/I_G that the average density of defects has increased by more than 2 times in ZrB$_2$–GNP composites reinforced with 2 and 4 vol% GNPs. The density of defects is comparatively higher in 2 vol% than 4 and 6 vol% GNP reinforced composites and it scales inversely with the concentration of GNPs. In general, high temperature (> 1600 °C) sintering of nanocrystalline graphite increases the average crystallite size [47]. This situation is directly observed in sintering of pure GNPs. The I_D/I_G value of sintered GNPs is close to zero (Fig. 6a) which is reminiscent of crystalline graphite. This point is further corroborated by *G* peak position being at 1581 cm^{-1} (Fig. 6a), which is in close agreement with literature [41]. Hence, it is inferred that I_D/I_G has increased for ZrB$_2$ composites because of interfacial reactions between GNPs and ZrB$_2$ matrix at high SPS processing temperature (1900 °C). I_D/I_G is higher at low concentrations of GNPs possibly due to two reasons: (i) less GNP aggregation and therefore, more carbon surface interaction with ZrB$_2$ per GNP; and (ii) higher multiplication of GNPs due to exfoliation at lower GNP concentration. The exfoliation of GNPs provides more GLs in contact with ZrB$_2$ matrix in 2 and 4 vol% GNP reinforced composites and it will result in a higher I_D/I_G [48]. This point is supported by the positions of *G* and *G*′ peak.

In addition, the *G* peak frequency in ZrB$_2$–GNP (2, 4 and 6 vol%) for corresponding I_D/I_G values is expected to decrease simultaneously with increasing concentration of GNPs [43]. According to Ferrari et al., when the I_D/I_G value increases from 0 to 2 due to increasing concentration of defects in nanocrystalline graphite, a high energy shift of the *G* peak from 1580 to 1600 cm^{-1} is observed concomitantly [41]. On the contrary, we observe the *G* peak frequencies at 1584 and 1585 cm^{-1} for 2 and 4 vol% GNPs reinforced composites, respectively (Fig. 6a). This shift is lower than the expected G peak shift by 6 and 5 cm^{-1}, respectively (estimated from Ref. 43 using corresponding I_D/I_G values of 2 and 4 vol% GNPs). This discrepancy is attributed to reduction in nGLs in GNPs of 2 and 4 vol% reinforced composites that occurred due to exfoliation [48,49]. On the other hand, the *G* peak of 6 vol% GNP reinforced composite (at 1588 cm^{-1}) has shifted to higher energy than expected *G* peak (1583 cm^{-1}) that is suggestive of the residual compressive stresses acting on GNPs incurred during thermal contraction of ZrB$_2$ matrix [43–45]. The thermal stresses are more prominent in 6 vol% than 2 vol% GNP reinforced composite due to higher densification of the ceramic matrix. Concurrently, we observe a higher frequency shift in the *D* peak in 6 vol% GNP reinforced composite due to residual compressive stresses.

In order to investigate the process of exfoliation we focused on the *G*′ band. It is evident from Fig. 6(a), that the *G*′ band of the composites has shifted to lower energy. This lower shift in *G*′ band implies that the nGLs has decreased [48,49]. Alternatively, the shift in the *G*′ peak is also possible due to interfacial reactions incurred during the high temperature processing of composites. As discussed from the thermodynamic analysis, the possible interfacial reaction could be formation of ZrC or solid solution of ZrC in ZrB$_2$. Another possibility is the doping of GNPs with B atoms. Both possible interfacial interactions are expected to result in high energy shift in G' band [50]. On the other hand, we observe a low energy shift in the G' band that suggests reduction in nGLs has the dominant influence on the G' band frequency. To further investigate the origin behind exfoliation of graphene, we acquired Raman spectra in ball-milled GNPs with and without ZrB_2 powder as shown in Fig. 6(b). The lower energy shift in the G' band indicates a decrease in nGLs during ball-milling. In addition, the trend in I_D/I_G as well as G peak frequency suggests that the ball-milling has induced minimal damage. Additional shift in the G' band of sintered composite suggests further decrease in nGLs during SPS processing of the ball-milled mixture of ZrB_2 and GNPs.

3.3. Mechanical properties

The variation of indentation hardness with GNP reinforcement content in the ZrB_2–GNP composites is presented in Fig. 7. Among all the compositions investigated in this study, the monolithic ZrB_2, with ~85% relative density, exhibited highest average hardness of about 16.6 GPa. Even though ZrB_2–GNP composites exhibited higher relative density, no improvement in the hardness was observed with GNP reinforcement in the composites. In fact, the hardness of composites was relatively lower compared to that of monolithic ZrB_2. The average hardness of the composites (2–6 vol% GNPs) was in the range of 15.5–15.9 GPa without any specific trend with increasing GNP reinforcement content. The lower hardness of the composites could be due to competing effects of densification, GNP induced strengthening, grain growth, and interfacial reactions on the hardening of ceramics. On the other hand, all the composites showed improved biaxial flexural strength compared to the monolithic ZrB_2 (Fig. 8). The monolithic ZrB_2 had the average flexural strength of about 162 MPa. The ZrB_2–GNP composites reinforced with 2 and 4 vol% GNPs had the flexural strength of about 204 and 219 MPa, respectively. The composites reinforced with 6 vol% GNPs exhibited highest flexural strength (316 MPa), which is about two times that of monolithic ZrB_2. Clearly, the biaxial flexural strength, which better represents the strength-related property of the bulk samples than the surface microhardness, shows much better correlation with the GNP reinforcement content or the relative density of the ZrB_2–GNP composites. Fig. 9 shows the variation of indentation fracture toughness of the ZrB_2–GNP composites with GNP reinforcement content. The fracture toughness of monolithic ZrB_2 samples (1.5 MPa $m^{1/2}$) is also indicated in the figure. The fracture toughness values reported here for monolithic ZrB_2 samples are relatively lower than those reported for nearly fully dense ZrB_2 samples (3–4 MPa $m^{1/2}$). In general, the fracture toughness of the composites was higher than that of monolithic ZrB_2 and increased with increasing GNP content. Among all the composite compositions investigated, the ZrB_2–GNP composites reinforced with 6 vol% GNPs exhibited highest average fracture toughness of 2.8 MPa $m^{1/2}$, an increase of about 83% over the monolithic ZrB_2. While toughening effect of GNPs is clearly observed, the measurement of crack lengths using SEM seems to have resulted in underestimation of fracture toughness. Note that there are controversies surrounding the use of indentation methods for characterizing fracture toughness of ceramics reinforced with nano-scale fillers [51–53]. The indentation fracture toughness values obtained by indentation methods may not be representative of the bulk samples due to complexity of stress conditions associated with indentation process. For better characterization of the fracture toughness of the GNP reinforced ceramic samples, single edge V-notch bending (SEVNB) and rising R-curve methods will be used [53]. SEM micrographs showing morphologies of cracks emanated from the indentation corners for ZrB_2 and ZrB_2–GNP composites are presented in Fig. 10. The crack front was relatively straight for monolithic ZrB_2 samples without significant toughening mechanisms such as crack deflection or bending (Fig. 10(a)). In these samples, the cracks propagate along the grain boundaries and meet

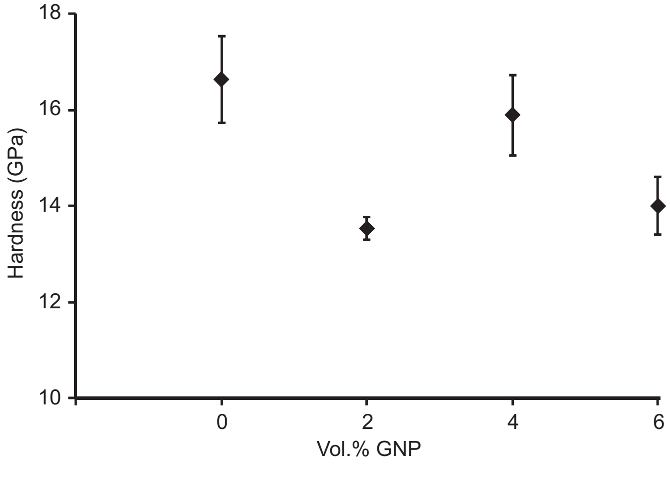

Fig. 7. Hardness of ZrB_2–GNP composites as a function of GNP reinforcement content.

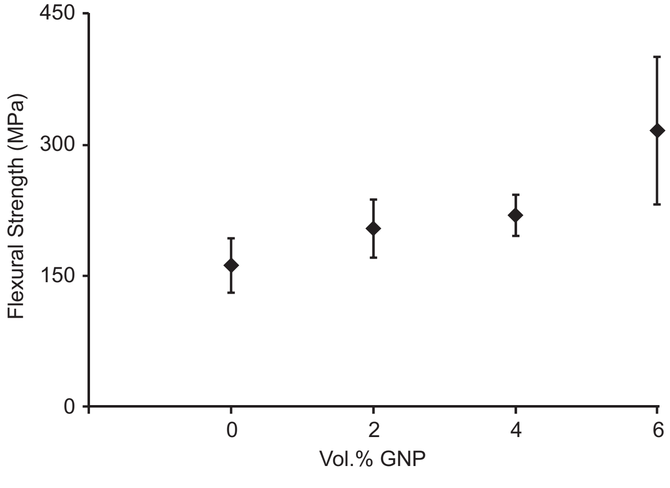

Fig. 8. Flexural strength of ZrB_2–GNP composites as a function of GNP reinforcement content.

open porosity of the samples. The SEM micrograph from the fracture surface indicated clear intergranular fracture in these porous (relative density of about 85%) ZrB_2 samples (Fig. 2(a)). For the ZrB_2–GNP composites (2 vol% GNPs), the morphology of the indentation cracks is similar to that for ZrB_2 samples except that the cracks encounter agglomerates of GNPs. The GNP agglomerates at the grain boundaries seem to deflect the cracks along the grain boundaries leading to intergranular fracture (Figs. 10(b) and 2(b)). In ZrB_2–GNP composites with higher amount of GNP reinforcement (4 and 6 vol%), the indentation cracks propagated both along the grain boundaries and through the grains with crack deflection at the graphene agglomerates at the grain boundaries (Fig. 10(c,d)). The fracture surface also shows flatter surface features with predominantly transgranular fracture through relatively coarse grains (Fig. 2(c,d)). The figure clearly shows the pulled out graphene plates at the grain boundary (Fig. 2(c)). The graphene plates wrapped along the grain boundaries over multiple grains can also be seen in the composite sample reinforced with 6 vol% GNPs (Fig. 2(d)). The difference in focus between lower left and upper right regions of this micrograph (Fig. 2(d)) indicate crack deflection at the graphene plates at the grain boundaries. The graphene plates also seem to bridge the indentation crack propagating perpendicular to the plates as seen in Fig. 11. While the ZrB_2–GNP composite samples exhibited relatively higher relative density and grain size than monolithic ZrB_2 samples, the fracture surfaces clearly indicate toughening mechanisms such as crack deflection and crack bridging with the reinforcement of GNPs in the composites. The effect of grain size on toughening in ceramics is often very weak. As the ZrB_2–GNP composites reinforced with 4 and 6 vol% GNPs exhibited fairly similar relative density (about 97%), higher indentation fracture toughness of composite reinforced with 6 vol% GNPs is indicative of increased contribution of GNPs in toughening the ceramic.

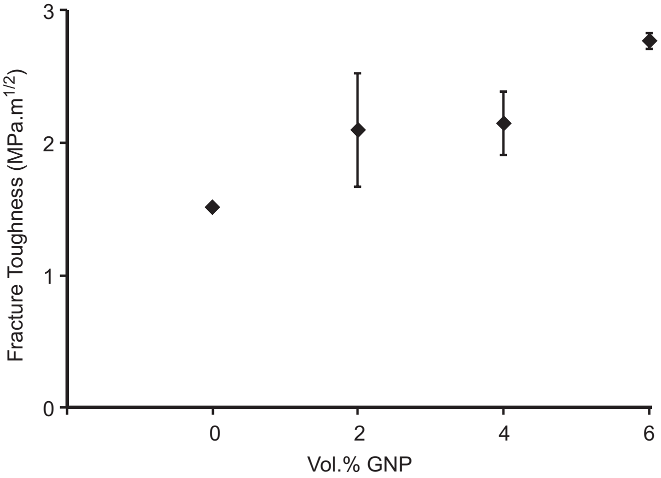

Fig. 9. Fracture toughness of ZrB_2–GNP composites as a function of GNP reinforcement content.

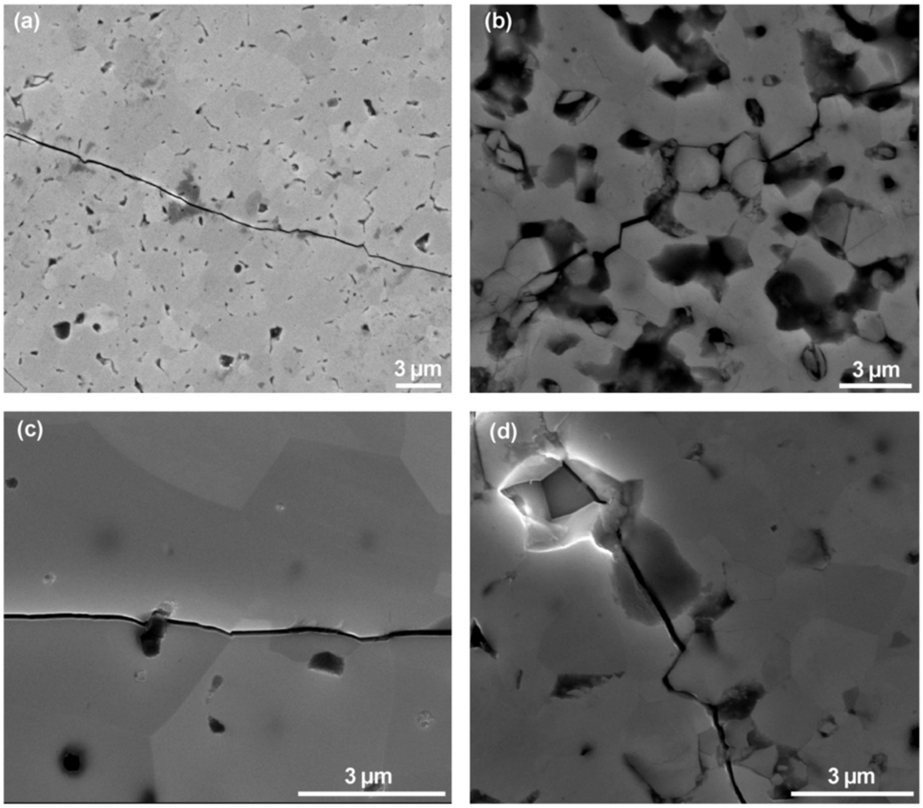

Fig. 10. Morphologies of indentation cracks for (a) monolithic ZrB_2, (b) ZrB_2–2% GNPs, (c) ZrB_2–4% GNPs, and (d) ZrB_2–6% GNPs composites.

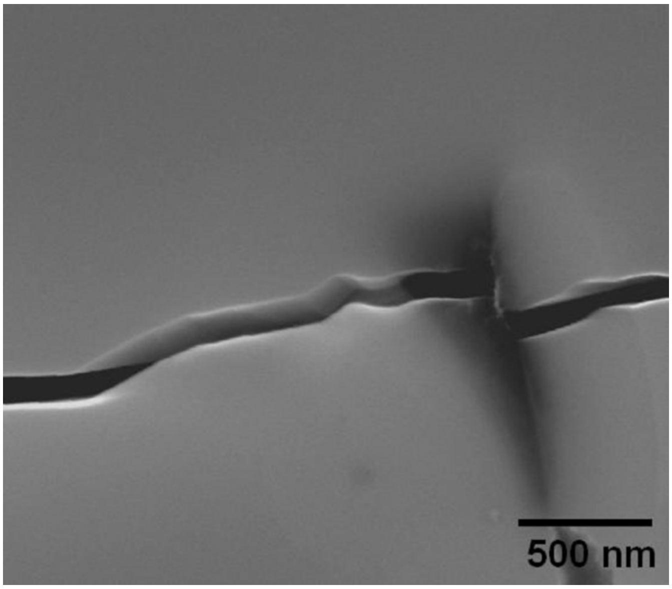

Fig. 11. A high magnification SEM micrograph showing bridging and deflection of an indentation crack front by graphene nanoplates.

4. Conclusions

Graphene nanoplate (GNP) reinforced ZrB_2 ultra-high temperature ceramic composites were successfully sintered using spark plasma sintering. In-process punch displacement profiles and thermodynamic analysis indicated that the reinforcement of GNPs favors the densification of composites, seemingly through interfacial reactions. Raman spectroscopy analysis indicated that the GNPs, with some extent of exfoliation or interfacial reactions, can be retained in the composites sintered at high temperature of 1900 °C. The analysis of the ratio of D and G band intensities (I_D/I_G) indicated that the average defect density in graphitic carbon has increased by more than 2 times for ZrB_2–GNP composites and it scales inversely with the concentration of GNPs. The I_D/I_G has increased for ZrB_2 composites because of interfacial reactions between GNPs and ZrB_2 matrix, leading to removal of oxide impurities or formation of ZrC, at high SPS processing temperature (1900 °C). Toughening effects of GNPs such as crack deflection and crack bridging were directly observed from high magnification images of the fracture surfaces and indentations crack morphologies.

Acknowledgment

The corresponding author SPH acknowledge support from the Oklahoma Space Grant Consortium through NASA-EPSCoR Research Initiation Grants program.

References

[1] M.J. Gasch, D.T. Ellerby, S.M. Johnson, Ultra high temperature ceramic composites, in: N. Bansal (Ed.), Handbook of Ceramic Composites, Kluwer Academic Publishers, Boston, 2005, pp. 197–224.
[2] M. Gasch, S. Johnson, Physical characterization and arcjet oxidation of hafnium-based ultra high temperature ceramics fabricated by hot pressing and field-assisted sintering, Journal of the European Ceramic Society 30 (2010) 2337–2344.
[3] M.M. Opeka, I.G. Talmy, E.J. Wuchina, J.A. Zaykoski, S.J. Causey, Mechanical, thermal, and oxidation properties of refractory hafnium and zirconium compounds, Journal of the European Ceramic Society 19 (1999) 2405–2414.
[4] E.L. Courtright, H.C. Graham, A.P. Katz, R.J. Kerans, Ultra high temperature assessment study-ceramic matrix composites, AFWAL-TR-91-4061, Ohio, Wright Patterson air Force Base, 1992.
[5] C. Mroz, Annual mineral review: zirconium diboride, American Ceramic Society Bulletin 74 (1995) 165–166.
[6] K. Upadhya, M.J. Yang, W.P. Hoffmann, Materials for high temperature applications, American Ceramic Society Bulletin 58 (1997) 51–56.
[7] F. Monteverde, A. Bellosi, S. Guicciardi, Processing and properties of zirconium diboride-based composites, Journal of the European Ceramic Society 22 (2002) 279–288.
[8] M.I. Low, R. McPherson, Fabrication of new zirconium boride ceramics, Journal of Materials Science Letters 8 (1989) 1281–1283.
[9] A.L. Chamberlian, W.G. Fahrenholtz, G.E. Hilmas, D.T. Ellerby, High-strength zirconium diboride-based ceramics, Journal of the American Ceramic Society 87 (2004) 1170–1172.
[10] H. Wang, C.A. Wang, X. Yao, D. Fang, Processing and mechanical properties of zirconium diboride-based ceramics prepared by spark plasma sintering, Journal of the American Ceramic Society Bulletin 90 (2007) 1992–1997.
[11] F. Monteverde, Beneficial effects of an ultra-fine α-SiC incorporation on the sinterability and mechanical properties of ZrB_2, Applied Physics A: Materials Science and Processing 82 (2006) 329–337.
[12] I. Akin, M. Hotta, F.C. Sahin, O. Yucel, G. Goller, T. Goto, Microstructure and densification of ZrB_2–SiC composites prepared by spark plasma sintering, Journal of the European Ceramic Society 29 (2009) 2379–2385.
[13] W.C. Tripp, H.H. Davis, H.C. Graham, Effect of an SiC addition on the oxidation of ZrB_2, American Ceramic Society Bulletin 52 (1973) 612–616.
[14] G.B. Yadhukulakrishnan, A. Rahman, S. Karumuri, M.M. Stackpoole, A.K. Kalkan, R.P. Singh, S.P. Harimkar, Spark plasma sintering of silicon carbide and multi-walled carbon nanotube reinforced zirconium diboride ceramic composite, Materials Science and Engineering A 552 (2012) 125–133.
[15] W.B. Tian, Y.M. Kan, G. Zhang, P.P. Wang, Effect of carbon nanotubes on the properties of ZrB_2–SiC ceramics, Materials Science and Engineering A 487 (2008) 568–573.
[16] J. Cho, A.R. Boccaccini, M.S.P. Shaffer, Ceramic matrix composites containing carbon nanotubes, Jouirnal of Materials Science 44 (2009) 1934–1951.
[17] S. Park, R.S. Ruoff, Chemical methods for the production of graphenes, Nature Nanotechnology 4 (2009) 217–224.
[18] A.K. Geim, K.S. Novoselvo, The rise of graphene, Nature Materials 6 (2007) 183–191.
[19] M. Segal, Selling graphene by the ton, Nature Nanotechnology 4 (2009) 612–614.
[20] A.A. Balandin, S. Ghosh, W. Bao, I. Calizo, D. Teweldebrhan, F. Miao, C.N. Lau, Superior thermal conductivity of single-layer graphene, Nano Letters 8 (2008) 902–907.
[21] C. Lee, X. Wei, J.W. Kysar, J. Hone, Measurement of the elastic properties and intrinsic strength of monolayer graphene, Science 321 (2008) 385–388.
[22] C. Soldano, A. Mahmood, E. Dujardin, Production, properties and potential of graphene, Carbon 48 (2010) 2127–2150.
[23] Y. Zhang, J.P. Small, W.V. Pontius, P. Kimm, Fabrication and electric-field-dependent transport measurements of mesoscopic graphite devices, Applied Physics Letters 86 (2005) 073104.

[24] K.S. Novoselvo, A.K. Geim, J.D. Katsnelson, I.V. Grigorieva, A.A. Firsov, Electric field effect in atomically thin carbon films, Science 306 (2004) 666–669.

[25] K.S. Novoselov, E. McCann, S.V. Morozov, V.I. Fal′ko, M.I. Katsnelson, U. Zeitler, Unconventional quantum Hall effect and Berry's phase of 2π in bilayer graphene, Nature Physics 2 (2006) 177–180.

[26] O. Tapaszto, L. Tapaszto, M. Marko, F. Kern, R. Gadow, C. Balazsi, Dispersion patterns of graphene and carbon nanotubes in ceramic matrix composites, Chemical Physics Letters 511 (2011) 340–343.

[27] S. Stankovich, D.A. Dikin, G.H.B. Dommet, K.M. Kohlhass, E.J. Zimney, E.A. Stach, Graphene-based composite materials, Nature 442 (2006) 282–286.

[28] U. Khan, P. May, A. O′Neill, N.J. Coleman, Development of stiff, strong, yet tough composites by the addition of solvent exfoliated graphene to polyurethane, Carbon 48 (2010) 4035–4041.

[29] T. Ramanathan, A.A. Abdala, S. Stankovich, D.A. Dikin, M. Herrera-Alonso, R.D. Piner, Functionalized graphene sheets for polymer nanocomposites, Nature Nanotechnology 3 (2008) 327–331.

[30] M.A. Rafiee, J. Rafiee, Z. Wang, H. Song, Z.Z. Yu, N. Koratkar, Enhanced mechanical properties of nanocomposites at low graphene content, ACS Nano 3 (2009) 3884–3890.

[31] L.S. Walker, V.R. Marotto, M.A. Rafiee, N. Koratkar, E.L. Corral, Toughening in graphene ceramic composites, ACS Nano 5 (2011) 3182–3190.

[32] P. Kun, O. Tapaszto, F. Weber, C. Balazsi, Determination of structural and mechanical properties of multilayer graphene added silicon nitride-based composites, Ceramics International 38 (2012) 211–216.

[33] J. Wang, Z. Li, G. Fan, H. Pan, Z. Chen, G. Zhang, Reinforcement with graphene nanosheets in aluminum matrix composites, Scripta Materialia 66 (2012) 594–597.

[34] W. Zhang, I. Srivastava, Y.F. Zhu, C.R. Picu, N. Koratkar, Heterogeneity in epoxy nanocomposites initiates crazing: significant improvements in fatigue resistance and toughening, Small 5 (2009) 1403–1407.

[35] M.V. Antisari, A. Montone, N. Jovic, E. Piscopiello, C. Alvani, L. Pilloni, Low energy pure shear milling: a method for the preparation of graphite nano-sheets, Scripta Materialia 55 (2006) 1047–1050.

[36] K.A. Khalil, S.W. Kim, Effect of processing parameters on the mechanical and microstructural behavior of ultra-fine Al_2O_3-(ZrO_2+8% mol Y_2O_3) bioceramic, densified by high-frequency induction heat sintering, International Journal of Applied Ceramic Technology 3 (2006) 322–330.

[37] J.E.O. Ovri, A parametric study of the biaxial strength test for brittle materials, Materials Chemistry and Physics 66 (2000) 1–5.

[38] S. Zhu, W.G. Fahrenholtz, G.E. Hilmas, S.C. Zhang, Pressureless sintering of carbon-coated zirconium diboride powders, Materials Science and Engineering A 459 (2007) 167–171.

[39] J. Ado, M.S. Dresselhaus, S. Ricchiro, G.F. Dresselhaus, Raman Spectroscopy in Graphene Related Systems, Wiley-VCH Verlag, Germany, 2011.

[40] M.S. Dresselhaus, A. Jorio, M. Hofmann, G. Dresselhaus, R. Saito, Perspectives on carbon nanotubes and graphene raman spectroscopy, Nano Letters 10 (2010) 751–758.

[41] A.C. Ferrari, J. Robertson, Interpretation of Raman spectra of disordered and amorphous carbon, Physical Review B 61 (2000) 14095–14107.

[42] X. Wang, N.P. Padture, H. Tanaka, Contact-damage-resistant ceramic/single-wall carbon nanotubes and ceramic/graphite composites, Nature Materials 3 (2004) 539–544.

[43] P.M. Ajayan, L.S. Schadler, C. Giannaris, A. Rubio, Single-walled carbon nanotube–polymer composites: strength and weakness, Advanced Materials 12 (2000) 750–753.

[44] G. Tsoukleri, J. Parthenios, K. Papagelis, R. Jalil, A.C. Ferrari, A.K. Geim, Subjecting a graphene monolayer to tension and compression, Small 5 (2009) 2397–2402.

[45] A. Gupta, G. Chen, P. Joshi, S. Tadigadapa, P.C. Eklund, Raman scattering from high-frequency phonons in supported n-graphene layer films, Nano Letters 6 (2006) 2667–2673.

[46] A.C. Ferrari, J.C. Meyer, V. Scardaci, C. Casiraghi, M. Lazzeri, F. Mauri, Raman spectrum of graphene and graphene layers, Physical Review Letters 97 (2006) 187401.

[47] K. Takai, M. Oga, H. Sato, T. Enoki, Y. Ohki, A. Taomoto, Structure and electronic properties of a nongraphitic disordered carbon system and its heat-treatment effects, Physical Review B 67 (2003) 214202.

[48] J. Ado, M.L. Marcia, S. Fernando, H.M.F. Erlon, V.O.M. Marcus, B.C. Rodrigo, A.A. Carlos, Raman study of ion-induced defects in N-layer graphene, Journal of Physics: Condensed Matter 22 (2010) 334204.

[49] E.H. Martins Ferreira, M.V.O. Moutinho, F. Staval, M.M. Lucchese, R.B. Capaz, C.A. Achete, A. Jorio, Evolution of the Raman spectra from single-, few-, and many-layer graphene with increasing disorder, Physical Review B 82 (2010) 125429.

[50] A. Das, S. Pisana, B. Chakraborty, S. Piscanec, S.K. Saha, U.V. Waghmare, Monitoring dopants by Raman scattering in an electrochemically top-gated graphene transistor, Nature0 Nanotechnology 3 (2008) 210–215.

[51] D.T. Jiang, K. Thomson, J.D. Kuntz, J.W. Ager, A.K. Mukherjee, Effect of sintering temperature on a single-wall carbon nanotube-toughened alumina-based nanocomposite, Scripta Materialia 56 (2007) 959–962.

[52] N.P. Padture, W.A. Curtin, Comment on Effect of sintering temperature on single-wall carbon nanotube toughened alumina-based composite, Scripta Materialia 58 (2008) 989–990.

[53] D. Jiang, A.K. Mukherjee, Response to comment on Effect of sintering temperature on single-wall carbon nanotube toughened alumina-based nanocomposite, Scripta Materialia 58 (2008) 991–993.